TU Delft

Delft University of Technology

Document Version
Final published version

Licence
Dutch Copyright Act (Article 25fa)

Citation (APA)
Radovskaia, V., Andrei, R., Hortensius, J. R., Mikhaylovskiy, R. V., Citro, R., Chattopadhyay, S., Ivanov, B. A., Caviglia, A. D., Afanasiev, D., & More Authors (2026). Photoengineering the magnon spectrum in an insulating antiferromagnet. *Nature Physics*, *22*(5), 728-735. https://doi.org/10.1038/s41567-026-03230-6

Important note
To cite this publication, please use the final published version (if applicable).
Please check the document version above.

Copyright
In case the licence states “Dutch Copyright Act (Article 25fa)”, this publication was made available Green Open Access via the TU Delft Institutional Repository pursuant to Dutch Copyright Act (Article 25fa, the Taverne amendment). This provision does not affect copyright ownership.
Unless copyright is transferred by contract or statute, it remains with the copyright holder.

Sharing and reuse
Other than for strictly personal use, it is not permitted to download, forward or distribute the text or part of it, without the consent of the author(s) and/or copyright holder(s), unless the work is under an open content license such as Creative Commons.

Takedown policy
Please contact us and provide details if you believe this document breaches copyrights.
We will remove access to the work immediately and investigate your claim.

This work is downloaded from Delft University of Technology.

nature physics

Article

https://doi.org/10.1038/s41567-026-03230-6

Photoengineering the magnon spectrum in an insulating antiferromagnet

Received: 1 May 2025

Accepted: 25 February 2026

Published online: 14 April 2026

Check for updates

V. Radovskaia[1] ✉, R. Andrei[2], J. R. Hortensius[3,4], R. V. Mikhaylovskiy[5], R. Citro[6], S. Chattopadhyay[2,7], M. X. Na[1], B. A. Ivanov[1,8], E. Demler[2], A. V. Kimel[1], A. D. Caviglia[9] & D. Afanasiev[1] ✉

In antiferromagnets, where quantum mechanical exchange interactions dictate spin behaviour, understanding the dynamics of magnons—collective spin wave excitations that naturally reach terahertz frequencies and supersonic velocities—is essential for both fundamental science and emerging technologies. Femtosecond optical pulses offer a powerful means to coherently excite these magnons across the full Brillouin zone and to manipulate their spectral characteristics. Yet, achieving such control has remained difficult, as it requires ultrafast and sustained tuning of the underlying exchange interaction. Here we demonstrate an optically driven renormalization of the terahertz magnon spectrum in the insulating antiferromagnet $DyFeO_3$. Our results show that this transformation arises from a substantial transient reduction of the exchange interaction within a nanoscale region near the surface. These findings reveal a route to light-induced, nanoscale control of antiferromagnetic spin dynamics, opening opportunities for reconfigurable, ultrafast magnonic and spintronic functionalities.

Femtosecond light pulses lead the exploration of spin dynamics in antiferromagnets (AFMs), materials with antiparallel spin ordering. In response to such rapid excitation, AFMs generate magnons—collective waves of spin precession at terahertz frequencies—offering exciting opportunities for high-speed and energy-efficient spintronics and magnonics applications[1–4]. Ultrashort pulses have been shown to drive coherent spin-wave excitations across the entire Brillouin zone, including zone-centre magnons[5], zone-edge two-magnon states[6] and, more recently, finite-momentum propagating modes[7–10]. Light has not only enabled the excitation of these modes but also revealed their nonlinear interactions[11–14], leading to a redistribution of energy and momentum across the entire magnon spectrum. Ultrafast photoengineering of the terahertz magnon spectrum is the next monumental challenge enabling precise control over magnon propagation and interactions on ultrafast timescales[15,16]. Achieving this crucially requires direct control of the most fundamental interaction in AFMs—the exchange interaction—which not only drives AFM magnon frequencies into the terahertz range but also establishes the quasi-linear relativistic dispersion relation between their frequency and momentum, thus enabling dispersionless propagation of AFM magnons at velocities exceeding those of sound and, consequently, of heat propagation[1,2,4].

Ultrafast optical control of exchange interactions has been widely studied in strongly correlated AFM systems, such as Mott–Hubbard and charge-transfer (CT) insulators. In these systems, local electron–electron correlations not only determine the nature of the insulating bandgap but also govern the strength of the AFM exchange[17]. Current approaches to optical control the exchange interaction rely on tuning electron wavefunction overlap—that is, hopping

[1]Institute for Molecules and Materials, Radboud University, Nijmegen, the Netherlands. [2]Institute for Theoretical Physics, ETH Zurich, Zurich, Switzerland. [3]Kavli Institute of Nanoscience, Delft University of Technology, Delft, the Netherlands. [4]Electromagnetic Signatures and Propagation, TNO, The Hague, the Netherlands. [5]Department of Physics, Lancaster University, Lancaster, UK. [6]Dipartimento di Fisica 'E. R. Caianiello', Università degli Studi di Salerno, CNR-SPIN, Fisciano, Italy. [7]Lyman Laboratory, Department of Physics, Harvard University, Cambridge, MA, USA. [8]Institute of Magnetism, National Academy of Sciences of Ukraine, Kyiv, Ukraine. [9]Department of Quantum Matter Physics, University of Geneva, Geneva, Switzerland.
✉e-mail: viktoriia.radovskaia@ru.nl; d.afanasiev@science.ru.nl

amplitudes—by below- or above-bandgap optical excitation[18–22]. While below-bandgap excitation enables reversible control of exchange interaction, the effects are short-lived, typically reduced to the optical pulse duration[18,21,23]. Recent experiments also suggest that such modifications are on the order of 1% and are primarily limited to impulsive excitations of coherent spin precession[19,22,24]. By contrast, near- or above-bandgap optical excitation creates a non-equilibrium distribution of photoexcited charge carriers. Theory predicts that, in the limit of strong electronic correlations, these carriers may relax into a non-thermal 'hidden' state, transiently modifying exchange interactions[25–28]. However, a direct impact on the coherent spin-wave spectrum has not yet been observed; instead, the primary effect remains the ultrafast melting of AFM order, driven by the collapse of local magnetic moments[29–33].

In this work, we investigate the impact of femtosecond laser excitation on the magnon dynamics in the CT insulating AFM oxide dysprosium orthoferrite ($DyFeO_3$), known for strong optomagnetic effects[34,35] and electronic correlations[36,37]. Using time- and momentum-resolved magnon spectroscopy, we show that, at the material's surface, above-bandgap excitation generates coherent AFM spin-waves with distinct spectral signatures absent in equilibrium. Most notably, we observe the emergence of a quasi-continuous spectral distribution of magnons at reduced frequencies or energies, resulting from a near-total collapse of the equilibrium magnon energy gap. This profound modification of the spin-wave spectrum leads to extraordinary large decay rate of the experimentally observed coherent spin-wave oscillations. Our theoretical model, incorporating key magnetic interactions, indicates that the observed spectral renormalization is driven by a long-lived, non-thermal electronic state confined to a photoexcited near-surface nanoscale layer, where exchange interactions are dramatically altered.

Magnon spectrum and electronic structure of AFM $DyFeO_3$

$DyFeO_3$ is an AFM insulator with a high Néel temperature of $T_N \approx 650$ K and strong electronic correlations[36,37]. Below T_N, the AFM hosts two distinct magnetic phases separated by a first-order phase transition at $T_M = 51$ K (ref. 38). In the low-temperature collinear AFM phase, the iron Fe^{3+} spin ($S = 5/2$) sublattices $\mathbf{S}_1$ and $\mathbf{S}_2$ are antiparallel, resulting in zero net magnetization. In the high-temperature weak ferromagnetic (WFM) phase, the spin–orbit-driven Dzyaloshinskii–Moriya (DM) interaction causes the iron spins to cant, resulting into the emergence of a net magnetization $\mathbf{M}$ along the z axis. The magnitude of this WFM moment is governed by the delicate competition between the large exchange interaction J, favouring antiparallel spin alignment, and the much smaller DM interaction D, such that $\mathbf{M} \propto D/J$ (see Supplementary Note 1 for a detailed discussion).

Our experiments on photoengineering the magnon spectrum in $DyFeO_3$ focus on the WFM phase, which hosts two magnon branches: the quasi-ferromagnetic (q-FM) and quasi-antiferromagnetic (q-AFM) modes. Among these, only the q-AFM mode is particularly sensitive to modifications of the exchange interaction (Supplementary Note 4). Indeed, its dynamics correspond to oscillations of the canting angle between neighbouring AFM spins, which modulate the magnitude of the net magnetization $\mathbf{M}(t)$ without changing its orientation. Because $\mathbf{M}$ itself arises from the ratio D/J, even small changes in J can trigger q-AFM dynamics and have a profound impact on its spectrum. Moreover, this mode undergoes a pronounced softening in the vicinity of T_M, further enhancing its susceptibility to modifications of the exchange interaction and making it an ideal probe of light-induced exchange renormalization.

Similar to other canted AFMs, the low-momentum dispersion of the q-AFM mode is well described by the relation[35,39]

$$f(k) = \sqrt{f_0^2 + (V_m k)^2} \quad (1)$$

relating the magnon frequency f to the linear wavenumber $k = 1/\lambda_{mag}$. The value V_m defines the so-called relativistic group velocity of AFM magnons in the limit of linear dispersion, away from the zone centre and edges; the lowest frequency f_0 is attributed to uniform spin precession ($k = 0$) and sets the magnon energy gap $E_0 = hf_0$. This magnon gap arises from the interplay of single-ion anisotropy and exchange interaction and—in orthoferrites—is highly sensitive to temperature through the anisotropy parameter[40]. By contrast, the velocity V_m is predominantly governed by the exchange interaction and remains nearly constant at $V_m \approx 20$ km s^{-1} across all temperatures[40]. Both f_0 and V_m can thus serve as an effective measures of the exchange interaction.

The valence and conduction bands of $DyFeO_3$ are primarily composed of oxygen 2p and iron 3d orbitals, respectively. Photoexcitation across the bandgap ($E_{CT} \approx 2.2$ eV) constitutes an electron transfer from an oxygen 2p orbital to a neighbouring iron 3d orbital (Fig. 1a). These CT transitions are crucial to the magnetic properties of $DyFeO_3$: in equilibrium, virtual CT processes mediate superexchange interactions between neighbouring iron ions, thereby establishing the AFM order[41,42]. Resonant pumping of the CT transitions has also been shown to promote the emission of coherent magnons[9,43,44]. Nevertheless, the effect of the excitation mechanism on the exchange interaction and on the spin-wave spectrum has remained elusive.

Anomalous magnon dynamics at $k \approx 0$

To start, we study the light-induced zone-centre ($k \approx 0$) coherent magnons in the WFM phase ($T = 55$ K) and compare the spin dynamics excited by pump pulses with photon energies from far below ($h\nu = 0.165$ eV) to above the CT bandgap ($h\nu = 3.1$ eV). To access their dynamics experimentally, we detect the pump-induced magneto-optical (MO) Faraday rotation θ_F of copropagating time-delayed probe pulses at $h\nu < E_{CT}$, which is sensitive to the dynamics of the magnetization $\mathbf{M}(t)$ along the z axis (Extended Data Fig. 1). Measured in the transmission geometry, θ_F captures a net component of the spin dynamics spatially integrated across the entire sample, which, in turn, encompasses all of the photoexcited volume.

Figure 1b shows that both types of optical excitation drive coherent oscillatory dynamics with frequency close to $f_0 \approx 0.16$ THz, corresponding to the $k \approx 0$ magnon mode of q-AFM type[39]. We did not observe any signs of the q-FM mode, whose frequency is known to be above 0.35 THz, that is, more than twice f_0 (ref. 39). Despite the similar frequencies, the decay rate γ of the q-AFM magnons is dramatically different: at $h\nu < E_{CT}$, γ coincides with $\gamma_0 = 0.003$ ps^{-1} for the q-AFM resonance[39], while at $h\nu > E_{CT}$, it yields $\gamma \approx 0.12$ ps^{-1}—nearly two orders of magnitude larger than γ_0. Fourier analysis (Fig. 1c) shows that the spectral density of the CT-induced magnon dynamics is substantially broader and exhibits a pronounced asymmetry. Plotting the spectral bandwidth Δf_{FWHM} of the optically excited magnons against the pump photon energy (Fig. 1d) reveals that varying $h\nu$ has almost no effect on Δf_{FWHM} for below-bandgap pumping ($h\nu \lesssim E_{CT}$). Upon onset of CT absorption, the value of Δf_{FWHM} rises rapidly. Not only does the spectral bandwidth of the spin excitation differ between below- and above-bandgap pumping, but the polarization dependence of the oscillation amplitude also changes. For $h\nu < E_{CT}$, the amplitude is strongly polarization dependent, consistent with optically induced magnetic anisotropy whose orientation is set by the pump polarization via the inverse Cotton–Mouton effect[45,46]. By contrast, resonant CT excitation at $h\nu > E_{CT}$ yields a polarization-independent spin response (Extended Data Fig. 2), indicating an excitation mechanism consistent with a modulation of the exchange as reported in refs. 21,22.

Note that below-bandgap pumping at $h\nu < E_{CT}$ exhibits negligible absorption, thereby uniformly exciting the sample across its entire thickness $d \approx 60$ μm. By contrast, CT excitation at $h\nu > E_{CT}$ is highly localized within a penetration depth $\delta \lesssim 100$ nm (ref. 9), considerably smaller than d. Thus, the anomalously short-lived magnon dynamics

https://doi.org/10.1038/s41567-026-03230-6

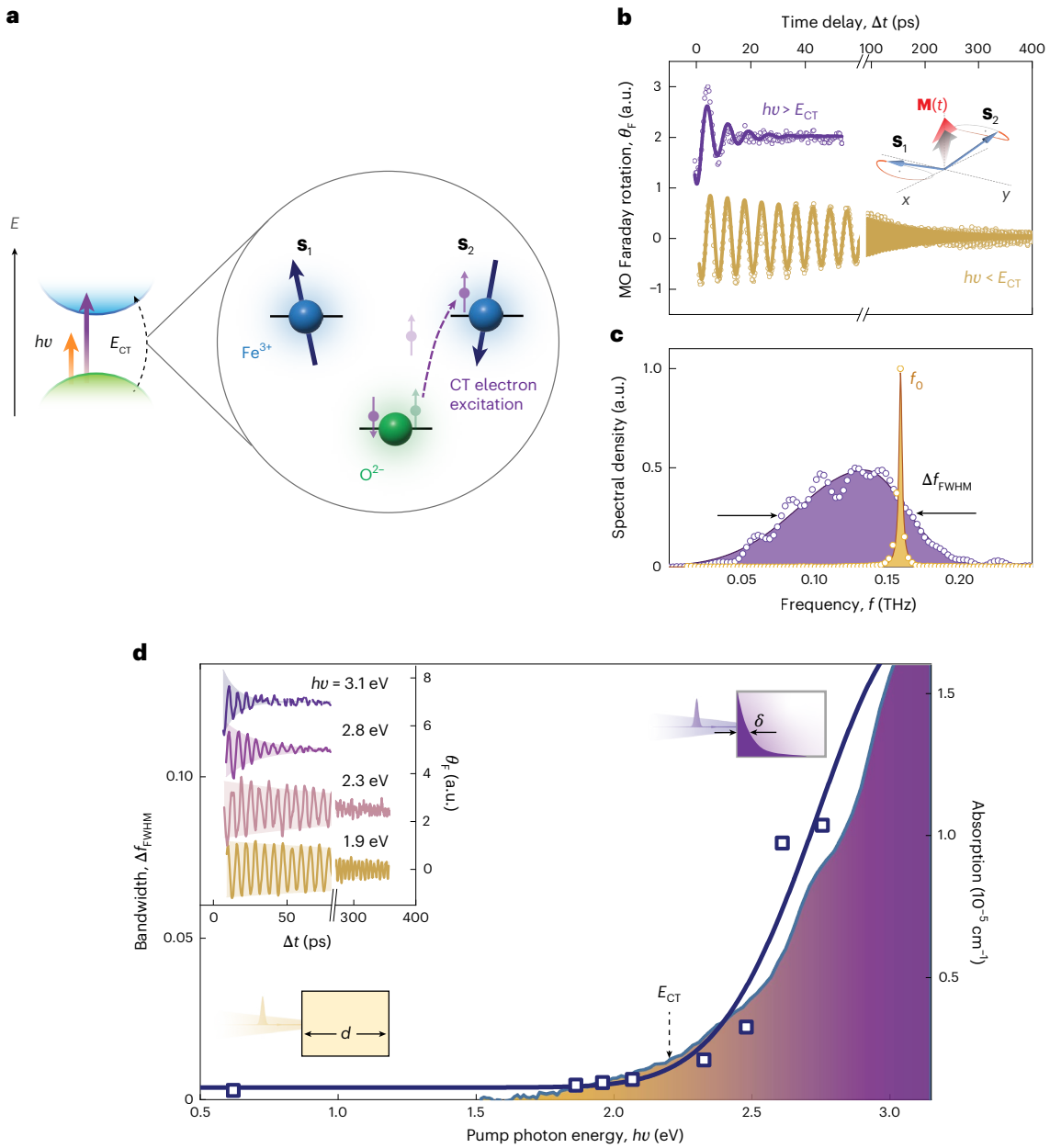


Fig. 1 | Anomalous magnon dynamics induced by selective pumping of CT transitions. a, A schematic illustrating CT electronic transitions between oxygen (green) and iron (blue) ions, which define the optical bandgap in $DyFeO_3$. **b**, Time-resolved traces of the MO Faraday rotation θ_F showing the coherent magnon dynamics at $k \approx 0$ for the optical pumping at the photon energy below ($h\nu = 0.165$ eV) and above ($h\nu = 3.1$ eV) the CT optical bandgap $E_{CT} = 2.2$ eV; the measurements were performed at $T = 55$ K; the probe was set to 1.55 eV. The inset illustrates a schematic representation of the q-AFM spin precession mode. **c**, Fourier transform showing the spectral density distribution of the time traces from **b**. f_0 denotes the frequency of $k \approx 0$ mode excited in the above CT bandgap regime. **d**, Left axis (squares): full width at half maximum (FWHM) spectral bandwidth Δf_{FWHM} of the pump-induced magnon dynamics as a function of $h\nu$. The solid purple line is a guide to the eye. Right axis: the colour-filled graph is an optical absorption profile of $DyFeO_3$; the colour gradient follows the pump photon energy from below-bandgap (yellow) to above-bandgap (purple) excitation for consistency. The top-left inset shows time-resolved traces of the pump-induced coherent magnon dynamics for various $h\nu$ across the CT bandgap. The bottom-left and top-right insets schematically illustrate the spatial distribution of the pump-induced spin excitation through the sample volume for the regimes $h\nu < E_{CT}$ (left) and $h\nu > E_{CT}$ (right).

and associated spectral broadening are related to the CT excitation localized to the sample surface.

Photoinduced continuum of in-gap magnon states

We further investigate how the strength of CT excitation influences the dynamics of localized $k \approx 0$ magnons in both time and frequency domains. Increasing the pump fluence F not only enhances the magnon amplitude but also drastically changes their temporal waveforms (Fig. 2a) and spectral profiles (Fig. 2b). In the low-fluence limit ($F = 0.6$ mJ cm^{-2}), the $k \approx 0$ magnon spectrum shows a narrow bandwidth ($\Delta f_{FWHM} < 0.02$ THz) symmetrically centred around the equilibrium magnon gap f_0, similar to the behaviour observed under below-bandgap pumping (Fig. 1c). The increasing pump fluence broadens the spectrum of the excited magnons, skews its spectral profile and redshifts the peak frequency f_p such that $f_p < f_0$ (Fig. 2b, inset). These results suggest that, near the sample surface, optical pumping of CT excitations generates a broadband quasi-continuum of coherent magnon states with frequencies falling well below the magnon gap. Due to their non-zero spatially

https://doi.org/10.1038/s41567-026-03230-6

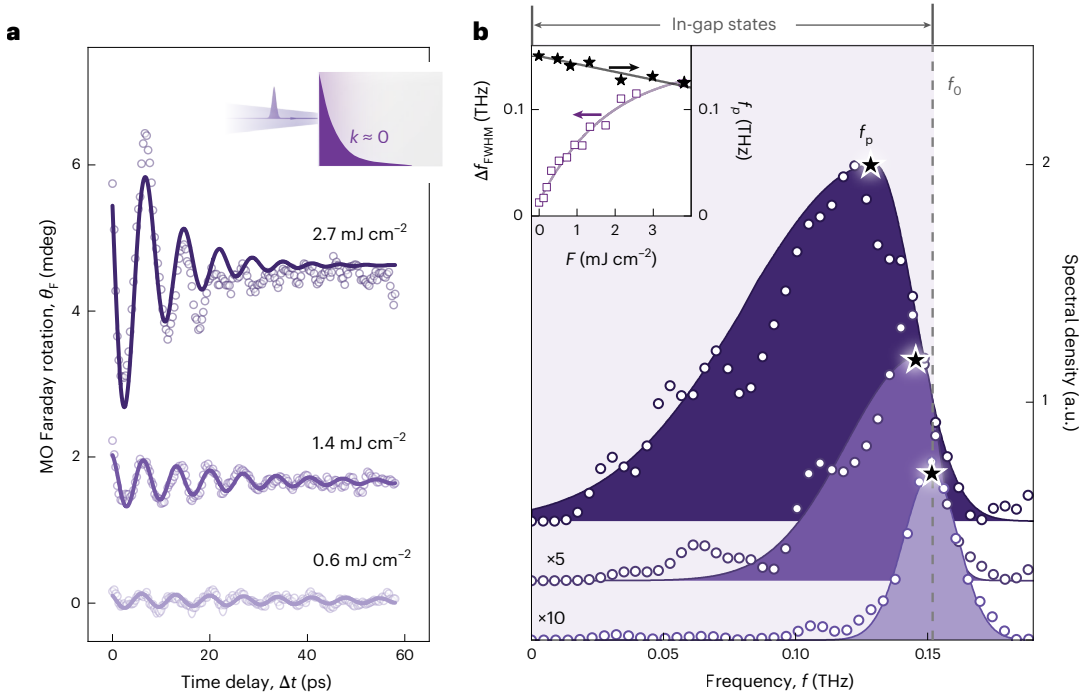


Fig. 2 | Photoinduced continuum of in-gap magnon states. a, Time-resolved traces of the MO Faraday rotation θ_F showing the coherent magnon dynamics at $k \approx 0$ for low ($F = 0.6$ mJ cm^{-2}), moderate ($F = 1.4$ mJ cm^{-2}) and strong ($F = 2.7$ mJ cm^{-2}) fluences of the above-bandgap pump excitation ($h\nu = 3.1$ eV). Circles are experimental data points; solid lines are the best fits with damped sine function. The mismatch between experimental data points and fits under high fluence indicates the asymmetrical reshaping of the spectra of the signal. The inset schematically shows spatial distribution of the measured dynamics localized within the optical penetration depth δ. **b**, Fourier transform showing the spectral density distribution of the time traces from **a**. Stars mark the peak frequencies f_p. The dashed grey line indicates magnon gap f_0, and the light-purple colour-filled area below f_0 represents in-gap states. The inset shows the evolution of the bandwidth Δf_{FWHM} (purple squares, left axis) and peak frequency f_p (black stars, right axis) of the excited magnon dynamics as a function of pump fluence. The measurements were performed at 53 K using a probe photon energy of 1.85 eV.

integrated amplitudes, these modes contribute to the MO Faraday signal, effectively mimicking $k \approx 0$ dynamics. The observed broadening thus reflects a presence of these new states, rather than intrinsic damping. Notably, as the pump fluence increases, the frequency range of the quasi-continuum also widens, resulting in a broader response.

Importantly, while above-bandgap optical excitation is accompanied by absorption and, thus, heating (Methods), the in-gap magnon continuum at $k \approx 0$ cannot be attributed to a pump-induced temperature rise. Even though in orthoferrites the value f_0 is strongly temperature dependent, in $DyFeO_3$ it does not fall below 0.14 THz (ref. 39). By contrast, the observed in-gap magnon states have much lower frequencies and, thus, are not thermally accessible. Furthermore, in the studied WFM phase, the frequency f_0 tends to increase with temperature (see ref. 46 and Extended Data Fig. 3) in contrast to the pump fluence-induced decrease in f_p. We also note that measurements in the AFM phase, where spin canting is absent, show no effect of the CT excitation on either the damping or the spectral properties of the magnons (Supplementary Note 5). The non-thermal nature of the observed magnon frequency changes, combined with the polarization-independent excitation mechanism and the absence of the effect in the collinear AFM phase, supports our hypothesis that CT excitation in $DyFeO_3$ renormalizes the exchange interaction, which, in turn, governs the spin-wave spectrum at $k \approx 0$.

Fingerprints of a photoengineered magnon band

Next, we investigate how the CT excitations affect magnon components with a finite momentum $k > 0$. These non-uniform components arise from the strong subwavelength localization of the CT excitation and are characterized by a finite bandwidth $\Delta k \approx \delta^{-1}$ (refs. 9,43,44). The corresponding finite-k excitations have non-zero group velocities $V_k = \partial f/\partial k \neq 0$ and, thus, rapidly escape the photoexcited region. Nonetheless, their early-time dynamics within $\tau_d \approx \delta/V_k$ may still provide valuable insights into the finite-k components of the magnon spectrum under the electronic excitation. To capture their dynamics, we performed time-resolved measurements of the MO Kerr effect (MOKE) in reflection geometry (Extended Data Fig. 1). In this configuration, MOKE provides access to a finite out-of-plane magnon momentum $\mathbf{k}_0$ which at normal incidence is given by $\mathbf{k}_0 = 2\mathbf{k}^*_{pr}$ where $\mathbf{k}^*_{pr}$ is the wavevector of the probe ray inside the material[9,47].

Figure 3a shows time-resolved traces of the MOKE rotation θ_K with an optical probe at $\lambda^1_{pr} = 515$ nm and $\lambda^2_{pr} = 670$ nm, revealing the magnon dynamics at $k_0 = k_1 \approx 0.94 \times 10^5$ cm^{-1} ($\lambda_1 \approx 110$ nm) and $k_0 = k_2 \approx 0.7 \times 10^5$ cm^{-1} ($\lambda_2 \approx 140$ nm), respectively. To compare the spectral response of $k = k_0$ magnons with those of $k \approx 0$, we mapped their Fourier spectra—acquired at the same temperature and pump fluence—onto the equilibrium magnon dispersion curve, $f(k)$ (Fig. 3b). While the finite-k spectra are dominated by the magnon component at the frequency $f(k_0) = f^1_k \approx 0.23$ and $f^2_k \approx 0.26$ THz, a broad spectral response centred around 0.1 THz is also clearly observed for all k. This low-frequency response, substantially lower than both f_k and f_0, closely matches the central frequency f_p of the spectrally renormalized oscillations at $k \approx 0$. Notably, it remains far above the frequency of the finite-k longitudinal acoustic phonons also detected in our experiments, ruling out a phononic origin (Extended Data Fig. 4).

The presence of spectral weight centred at $f_p < f_0$ at both $k \approx 0$ and $k = k_0$ suggests the formation of a strongly non-equilibrium magnon band around f_p. This band splits off from the original magnon spectrum and corresponds to an electronically modified magnetic state. Being localized within the pump penetration depth δ, this response extends to substantially larger momenta k.

https://doi.org/10.1038/s41567-026-03230-6

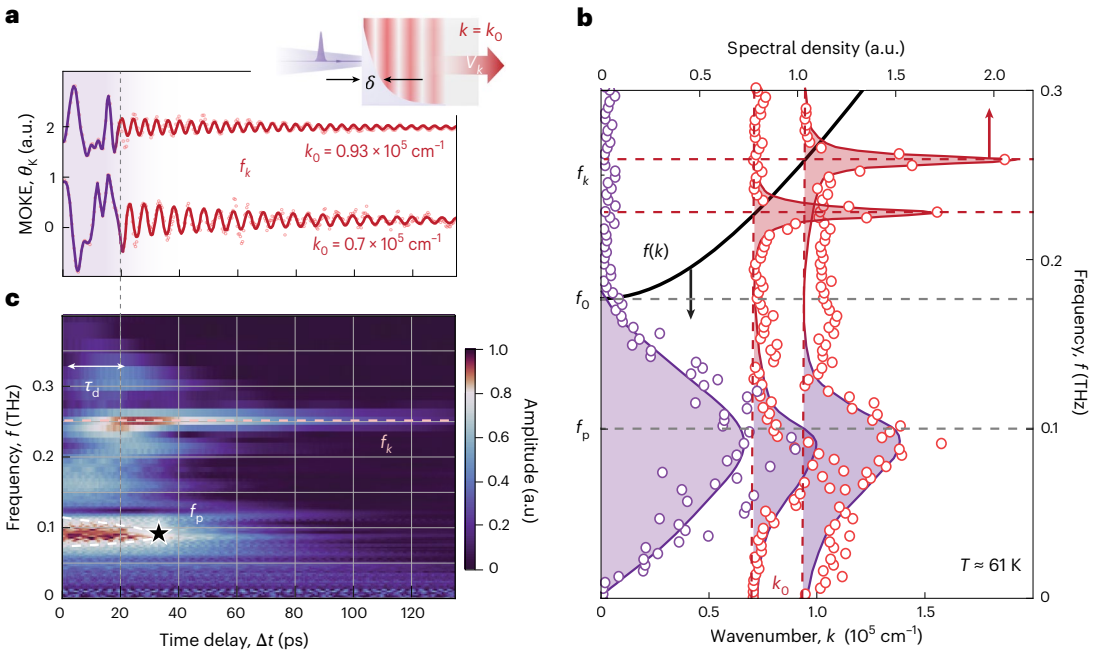


Fig. 3 | Fingerprints of a photoengineered magnonic band. a, Time-resolved traces of the MOKE rotation θ_K probing the coherent dynamics of finite-k components of the magnon packet excited by the above-bandgap pump excitation ($h\nu = 3.1$ eV). The probe wavelength set to 515 nm (top trace) and 670 nm (bottom trace) ensures selective detection of components at $k = k_1 = 0.94 \times 10^5$ and $k_2 = 0.7 \times 10^5$ cm^{-1} with the frequencies $f_k \approx 0.26$ and 0.23 THz, respectively. The shaded purple area highlights a distortion in the early-time dynamics of magnons at $k = k_0$. The dashed grey vertical line shows the early time τ_d in the f_k mode. The top-right inset schematically shows the spatial distribution of the probed magnon dynamics; δ is the pump penetration depth, and V_k is the group velocity of the propagating magnon. **b**, Fourier spectrum of $k \approx 0$ mode (purple, MO Faraday rotation) and $k = k_0$ (red, MO Kerr rotation) mapped on top of the equilibrium dispersion curve $f(k)$ (solid black line). The dashed red line marks f_k. Purple colour-filled areas below f_0 represent in-gap states. The upper (lower) dashed grey line marks the magnon gap f_0 (peak frequencies f_p). **c**, Wavelet analysis of the signal at $k = k_0 = 0.94 \times 10^5$ from **a**. The dashed pink line indicates the frequency f_k. The dashed white line highlights the evolution of the spectral density characterized by the peak frequency f_p in the early-time dynamics. The white arrow shows the early time τ_d in the f_k mode. The experiments were performed at $T = 61$ K, and pump fluence was set to $F = 6$ mJ cm^{-2}.

To understand the relationship between the spectral components at f_p and f_k, we performed a wavelet analysis of the finite-k magnon dynamics (Fig. 3c). This analysis reveals that, while the spatially localized signal at f_p emerges immediately after excitation, the spectral response at f_k, corresponding to propagating magnons, is delayed by $\tau_d \approx 20$ ps. This delay also manifests as an early-time distortion in the time-resolved waveforms (highlighted in Fig. 3a) and shows a strong correlation with the pump's penetration depth, δ (Extended Data Fig. 5). The delay suggests that the finite-k magnons originate from sample volume subjected to the CT excitation and, after exiting this region, freely propagate into the bulk of the sample according to the equilibrium dispersion. Indeed, our experiments show that—unlike the behaviour of localized components at f_p—the frequency and the decay rate of the f_k propagating component after τ_d are independent on the pump fluence (Extended Data Fig. 6). In this scenario, τ_d represents the time needed for the finite-k magnon to traverse the excited region, δ, and thus can be used to estimate the magnon velocity V_k^* within this electronically excited region. Surprisingly, our estimates show that $V_k^* \approx \delta/\tau_d \approx 5$ nm ps^{-1} —a few times smaller than the nominal $V_k \approx 15$ nm ps^{-1} for equilibrium magnon propagation. The reduced velocity provides further indication of a locally weakened exchange interaction in the optically excited near-surface region.

Localized state with renormalized magnetic interactions

To establish CT-driven renormalization of the exchange interaction as the primary mechanism for the photoinduced magnon band, and to rule out alternative scenarios, we consider a minimal model that replicates the observed magnon behaviour in $DyFeO_3$. The model is a three-dimensional bipartite spin lattice divided into sublattices 1 and 2, with principal magnetic interactions described by the microscopic Hamiltonian[38]

$$H = J_0 \sum_{i\in 1,\ \delta\in\{\pm\hat{x},\pm\hat{y},\pm\hat{z}\}} \mathbf{S}_i \cdot \mathbf{S}_{i+\delta} + D_0 \sum_{i\in 1,\ \delta\in\{\pm\hat{y}\}} (S^z{}_i S^x{}_{i+\delta} - S^x{}_i S^z{}_{i+\delta}) + \sum_{i\in 1,2} [K_2 (S^y{}_i)^2 - \frac{K_4}{S^2}(S^y{}_i)^4]. \quad (2)$$

The parameters J and D define the strength of the AFM superexchange and DM couplings, respectively. K_2 and K_4 represent the strengths of the quadratic and, respectively, quartic single-ion magnetic anisotropies that define the orientation of the iron spins. For exact values of the parameters, details of the considered Hamiltonian and the extended discussion of magnetic properties in thermal equilibrium, see Supplementary Note 1.

To simulate the effect of the CT excitation on the magnon spectrum, we introduce an effective spatiotemporal quench $Q(z,t)$ of the exchange interaction J_0, expressed as $J(z,t) = J_0\,(1 - Q(z,t))$. We estimate the temporal profile of the quench from transient reflectivity, which shows that the population of photoexcited carriers responsible for modifying the exchange persists well beyond the spin-precession period (Extended Data Fig. 7). We therefore model $Q(z,t)$ as a step function in time and exponentially decaying in space (Fig. 4a), with magnitude Q_0 scaling linearly with pump intensity. This minimal description captures both the dynamics within the excitation region and the outward propagation of magnons into the unperturbed volume (Fig. 4b).

The results of modelling spin dynamics for various Q_0 are shown in Fig. 4c (top). We present the quench-induced magnon dynamics as a

https://doi.org/10.1038/s41567-026-03230-6

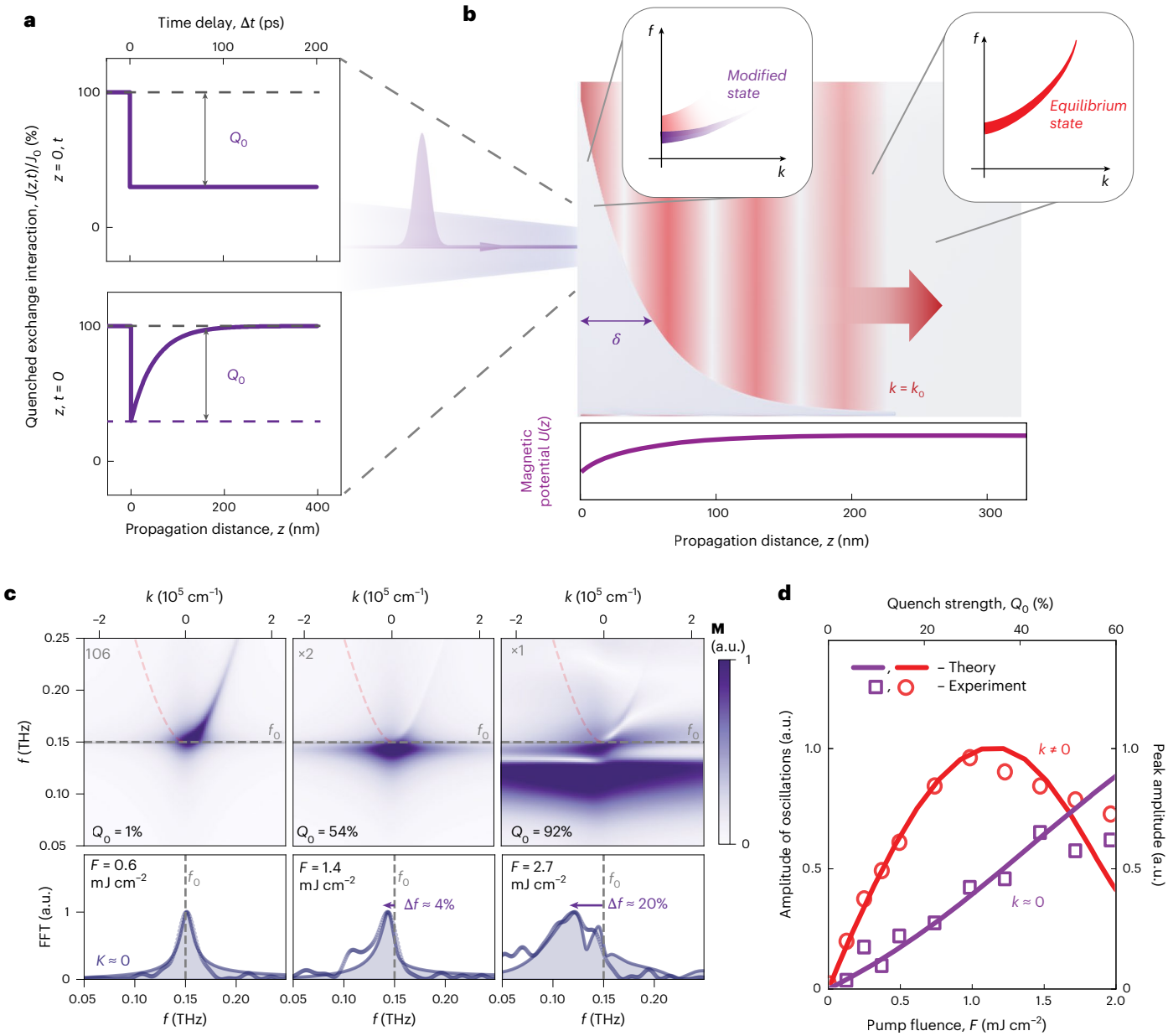


Fig. 4 | Ultrafast quench of exchange interaction. a, Temporal (top) and spatial (bottom) profile of quenching of the exchange interaction $J(z,t)/J_0$. Q_0 indicates the maximum quenching strength reached at the sample's surface. **b**, The schematic concept of the model considering that ultrafast CT excitation, via quenching of J, leads to the formation of a modified magnetic state localized within the excited area. Nevertheless, in the bulk, where J is unaffected, the magnetic state is equilibrium. Blue colour shows exponential absorbing profile; red colour represents propagating magnon with $k = k_0$ in the bulk. Top insets: schematic representation of the dispersions of modified and equilibrium states. Red colour shows equilibrium dispersion curve in the bulk, and purple colour shows modified dispersion curve inside excited area. Bottom inset: the violet solid line shows the magnetic potential well $U(z)$. **c**, Top: reciprocal space snapshots of the numerically calculated coherent dynamics of the amplitude of magnetization oscillation **M** in the arbitrary scale (magnification is specified in the top-left corner) for different quenching strengths Q_0. The dashed red line shows the equilibrium dispersion of spin waves. The straight dashed grey line shows the equilibrium magnon gap $f_0 = 0.15$ THz. Bottom: corresponding linear cuts (solid lines with filled area) from the snapshots at $k = 0$ from the top panel mapped on top of the experimental Fourier spectra (circles) of the $k \approx 0$ dynamics presented in Fig. 2b. The straight dashed grey line shows the equilibrium magnon gap $f_0 = 0.15$ THz. The purple arrow highlights the excitation-induced red shift of the spectral peak Δf that is observed in both experiment and theory. The exact values of Q_0 were selected to achieve the best fit of the experimental data using numerical calculations. **d**, Experimental values of the amplitude of oscillations as a function of pump fluence (symbols; left-bottom axes) plotted on top of the theoretical amplitude of the spectral peak as a function of the quench strength Q_0 (lines; right-top axes) for both $k \approx 0$ (purple) and $k \neq 0$ (red) magnon states.

two-dimensional Fourier transform mapped onto frequency–momentum space, which directly reveals the spectral distribution of excited magnons and allows straightforward comparison with the dispersion $f(k)$ (see equation (1)). The simulations show that suppression of J produces off-surface magnon emission with a k-space distribution set by the spatial profile of the quench. In the weak-quench regime (Fig. 4c, left), the effect is limited to a small perturbation near the surface, with spectral features following the equilibrium dispersion. At higher quench (Fig. 4c, middle and right), a broad spectral band emerges, extending across k-space and shifting to frequencies well below f_0, in line with the experimental data of Fig. 3c. This response is a direct consequence of the quench, and can be phenomenologically understood

as the emergence of localized magnon states near the surface, trapped by a spatially inhomogeneous potential (see below). Moreover, these near-surface magnons are characterized by reduced frequency and group velocity due to the suppression of the exchange interaction. We note that the frequency-broadening originates from the spatial profile of the quench $Q(z)$, which explores a range of different values in our region of interest; in the opposite case of spatially uniform $Q(z)$ = const, the broadening would be absent. To estimate the magnitude of the exchange quench reached in our experiment, we compare calculated line cuts at $k = 0$ with measured spectra shown in Fig. 2b. The fits shown in Fig. 4c (bottom) reproduce both the asymmetric broadening and the redshift below f_0. Notably, at $F \approx 2.7$ mJ cm^{-2}, the best agreement is obtained assuming a ~90% quench of the surface exchange interaction. This estimate is consistent with photoexcitation densities of ~10% carriers per unit cell, sufficient for a near-complete suppression of the effective exchange interaction J (Supplementary Note 2.1).

Remarkably, the quench scenario not only captures the main features of the magnon spectral modifications observed in experiments but also reproduces the non-trivial fluence dependence of both $k \approx 0$ and finite-k magnon amplitudes (Fig. 4d). Both theory and experiment show that, while the $k \approx 0$ mode grows superlinearly, the amplitude of propagating $k \neq 0$ magnons first levels off and then decreases at high fluence. Our analysis shows that this behaviour—including the previously discussed red frequency shift—arises from the local trapping of propagating spin-wave excitations. At high quench amplitudes, a deepened magnetic potential forms a near-surface potential well $U(z)$ (Fig. 4b, bottom inset) that reflects and thus locally traps finite-k magnons (with positive and negative wavenumbers) hindering their emission (Supplementary Note 3.2).

To further confirm that modification of the exchange interaction is the dominant factor driving our observed renormalization of the spin-wave spectrum, we exclude a wide range of possible alternatives. First, we theoretically explore ultrafast quenches of the other magnetic Hamiltonian terms. While modifications of the DM interaction D also affect the spin-wave spectrum, they fail to fully reproduce the experimental lineshape and fluence-dependent amplitudes (Supplementary Note 3.3). Meanwhile, simply modifying the anisotropies (K_2, K_4) fails to even trigger the spin dynamics (Supplementary Note 3.4), as it does not affect the D/J ratio. Although the optical excitation can still modify the strength of the anisotropy constants and thus reshape the spin wave spectrum, this reshaping is not fully consistent with our experiments (Supplementary Note 3.4). Second, we consider the reduction in size of local magnetic moments, a phenomenon that is to be expected upon photodoping strongly correlated insulators[29,48]. However, we argue that this effect is not only small but also qualitatively alters the spin-wave spectrum in a way that is inconsistent with experimental observations (Supplementary Note 3.5). Third, we examine amplitude-driven magnon interactions (Supplementary Note 3.6), as well as strong nonuniformities in the spatial profile of spin excitations (Supplementary Note 3.7), but in the absence of changes to any magnetic interactions. Neither scenario manages to capture the observed spectral renormalization, nor the amplitude behaviour, and thus both possibilities can be safely excluded. Together with the non-thermal nature of the spectral modifications, which has already been discussed, these arguments strongly support our interpretation of ultrafast light-induced modification to the exchange interaction in $DyFeO_3$.

Conclusions and outlook

Our findings extend the scope of resonant optical control in AFMs. We demonstrate that resonant pumping of CT electronic transitions—strongly coupled to fundamental spin exchange—not only quenches local magnetic moments, but also can be used to effectively reshape the magnon spectrum. Our results show that the renormalization of the magnon spectrum can be achieved by directly exciting electronic resonances, without destroying long-range magnetic order. This approach goes beyond previous strategies that relied primarily on nonlinear magnon–magnon interactions[11–14,47,49], including recent efforts involving direct terahertz excitation of two-magnon (2M) modes[49]. As many insulating AFMs belong to the class of CT systems, our discovery can be applied to a wide range of AFM materials[22,50] and may also provide insight into the microscopic mechanisms behind the optical generation of broadband terahertz magnon wavepackets in various iron oxides[9,43,44]. Nanoscale control of fundamental magnetic interactions, including exchange, opens new avenues for terahertz magnonics and spintronics, enabling the long-sought creation of dynamic AFM magnonic crystals[51,52]. On a fundamental level, our approach may enable enhanced dynamic interactions, such as magnon–magnon and magnon–phonon couplings, which are typically constrained by energy and momentum conservation limitations[53].

Online content

Any methods, additional references, Nature Portfolio reporting summaries, source data, extended data, supplementary information, acknowledgements, peer review information; details of author contributions and competing interests; and statements of data and code availability are available at https://doi.org/10.1038/s41567-026-03230-6.

References

1. Němec, P., Fiebig, M., Kampfrath, T. & Kimel, A. V. Antiferromagnetic opto-spintronics. *Nat. Phys.* **14**, 229–241 (2018).
2. Baltz, V. et al. Antiferromagnetic spintronics. *Rev. Mod. Phys.* **90**, 015005 (2018).
3. Han, J., Cheng, R., Liu, L., Ohno, H. & Fukami, S. Coherent antiferromagnetic spintronics. *Nat. Mater.* **22**, 684–695 (2023).
4. Dal Din, A., Amin, O. J., Wadley, P. & Edmonds, K. W. Antiferromagnetic spintronics and beyond. *NPJ Spintron.* **2**, 25 (2024).
5. Tzschaschel, C., Satoh, T. & Fiebig, M. Tracking the ultrafast motion of an antiferromagnetic order parameter. *Nat. Commun.* **10**, 3995 (2019).
6. Bossini, D. et al. Macrospin dynamics in antiferromagnets triggered by sub-20 femtosecond injection of nanomagnons. *Nat. Commun.* **7**, 10645 (2016).
7. Kainuma, R., Matsumoto, K., Ito, T. & Satoh, T. Sub-millimeter propagation of antiferromagnetic magnons via magnon-photon coupling. *NPJ Spintron.* **2**, 31 (2024).
8. Sun, Y. et al. Dipolar spin wave packet transport in a van der Waals antiferromagnet. *Nat. Phys.* **20**, 794–800 (2024).
9. Hortensius, J. R. et al. Coherent spin-wave transport in an antiferromagnet. *Nat. Phys.* **17**, 1001–1006 (2021).
10. Rongione, E. et al. Emission of coherent THz magnons in an antiferromagnetic insulator triggered by ultrafast spin–phonon interactions. *Nat. Commun.* **14**, 1818 (2023).
11. Zhang, Z. et al. Terahertz field-induced nonlinear coupling of two magnon modes in an antiferromagnet. *Nat. Phys.* **20**, 801–806 (2024).
12. Huang, C. et al. Extreme terahertz magnon multiplication induced by resonant magnetic pulse pairs. *Nat. Commun.* **15**, 3214 (2024).
13. Makihara, T. et al. Ultrastrong magnon–magnon coupling dominated by antiresonant interactions. *Nat. Commun.* **12**, 3115 (2021).
14. Li, X. et al. Observation of Dicke cooperativity in magnetic interactions. *Science* **361**, 794–797 (2018).
15. Krawczyk, M. & Grundler, D. Review and prospects of magnonic crystals and devices with reprogrammable band structure. *J. Phys. Condens. Matter* **26**, 123202 (2014).
16. Chumak, A. V., Vasyuchka, V. I., Serga, A. A. & Hillebrands, B. Magnon spintronics. *Nat. Phys.* **11**, 453–461 (2015).
17. Hubbard, J. Electron correlations in narrow energy bands. *Proc. R. Soc. A* **276**, 238–257 (1963).

18. Chaudhary, S., Hsieh, D. & Refael, G. Orbital Floquet engineering of exchange interactions in magnetic materials. *Phys. Rev. B* **100**, 220403 (2019).
19. Liu, J., Hejazi, K. & Balents, L. Floquet engineering of multiorbital Mott insulators: applications to orthorhombic titanates. *Phys. Rev. Lett.* **121**, 107201 (2018).
20. Mentink, J. H. & Eckstein, M. Ultrafast quenching of the exchange interaction in a Mott insulator. *Phys. Rev. Lett.* **113**, 057201 (2014).
21. Mentink, J. H. Manipulating magnetism by ultrafast control of the exchange interaction. *J. Phys. Condens. Matter* **29**, 453001 (2017).
22. Mikhaylovskiy, R. V. et al. Ultrafast optical modification of exchange interactions in iron oxides. *Nat. Commun.* **6**, 8190 (2015).
23. Mentink, J. H., Balzer, K. & Eckstein, M. Ultrafast and reversible control of the exchange interaction in Mott insulators. *Nat. Commun.* **6**, 6708 (2015).
24. Batignani, G. et al. Probing ultrafast photo-induced dynamics of the exchange energy in a Heisenberg antiferromagnet. *Nat. Photon.* **9**, 506–510 (2015).
25. Murakami, Y., Golež, D., Eckstein, M. & Werner, P. Photoinduced nonequilibrium states in Mott insulators. *Rev. Mod. Phys.* **97**, 035001 (2025).
26. Eckstein, M. & Werner, P. Thermalization of a pump-excited Mott insulator. *Phys. Rev. B* **84**, 035122 (2011).
27. Murakami, Y. et al. Charge, and η-spin separation in one-dimensional photodoped Mott insulators. *Phys. Rev. Lett.* **130**, 106501 (2023).
28. Eckstein, M., Kollar, M. & Werner, P. Thermalization after an interaction quench in the Hubbard model. *Phys. Rev. Lett.* **103**, 056403 (2009).
29. Ehrke, H. et al. Photoinduced melting of antiferromagnetic order in $La_{0.5}Sr_{1.5}MnO_4$ measured using ultrafast resonant soft X-ray diffraction. *Phys. Rev. Lett.* **106**, 217401 (2011).
30. Afanasiev, D. et al. Ultrafast spin dynamics in photodoped spin–orbit Mott insulator Sr_2IrO_4. *Phys. Rev. X* **9**, 021020 (2019).
31. Caviglia, A. D. et al. Photoinduced melting of magnetic order in the correlated electron insulator $NdNiO_3$. *Phys. Rev. B* **88**, 220401 (2013).
32. Först, M. et al. Spatially resolved ultrafast magnetic dynamics initiated at a complex oxide heterointerface. *Nat. Mater.* **14**, 883–888 (2015).
33. Ishihara, S. Photoinduced ultrafast phenomena in correlated electron magnets. *J. Phys. Soc. Jpn.* **88**, 072001 (2019).
34. Eremenko, V. V. & Kharchenko, N. F. Magneto-optics of antiferromagnets. *Phys. Rep.* **155**, 379–401 (1987).
35. Kimel, A. V. et al. Ultrafast non-thermal control of magnetization by instantaneous photomagnetic pulses. *Nature* **435**, 655–657 (2005).
36. Adams, D. J. & Amadon, B. Study of the volume and spin collapse in orthoferrite $LuFeO_3$ using LDA+U. *Phys. Rev. B* **79**, 115114 (2009).
37. Stoeffler, D. & Chaker, Z. First principles study of the electronic structure and magnetic properties of $YFeO_3$ oxide. *J. Magn. Magn. Mater.* **442**, 255–264 (2017).
38. Zvezdin, A. K. & Matveev, V. M. Theory of the magnetic properties of dysprosium orthoferrite. *Sov. Phys. J.* **50**, 543–548 (1979).
39. Balbashov, A., Volkov, A., Lebedev, S., Mukhin, A. & Prokhorov, A. High-frequency magnetic properties of dysprosium orthoferrite. *Zh. Eksp. Teor. Fiz.* **88**, 974–987 (1985).
40. Li, X., Kim, D., Liu, Y. & Kono, J. Terahertz spin dynamics in rare-earth orthoferrites. *Photon. Insights* **1**, R05 (2023).
41. Khomskii, D. I. *Transition Metal Compounds* (Cambridge Univ. Press, 2014).
42. Wood, D. L., Remeika, J. P. & Kolb, E. D. Optical spectra of rare-earth orthoferrites. *J. Appl. Phys.* **41**, 5315–5322 (1970).
43. Yang, D. et al. Spin-orbit torque manipulation of sub-terahertz magnons in antiferromagnetic α-Fe_2O_3. *Nat. Commun.* **15**, 4046 (2024).
44. Leenders, R. A., Afanasiev, D., Kimel, A. V. & Mikhaylovskiy, R. V. Canted spin order as a platform for ultrafast conversion of magnons. *Nature* **630**, 335–339 (2024).
45. Kalashnikova, A. M. Impulsive generation of coherent magnons by linearly polarized light in the easy-plane antiferromagnet $FeBO_3$. *Phys. Rev. Lett.* **99**, 167205 (2007).
46. Afanasiev, D. et al. Control of the ultrafast photoinduced magnetization across the Morin transition in $DyFeO_3$. *Phys. Rev. Lett.* **116**, 097401 (2016).
47. Leenders, R. A. & Mikhaylovskiy, R. V. Theory of optical generation and detection of propagating magnons in an antiferromagnet. *Phys. Rev. B* **107**, 094423 (2023).
48. Dean, M. P. M. et al. Ultrafast energy- and momentum-resolved dynamics of magnetic correlations in the photo-doped Mott insulator Sr_2IrO_4. *Nat. Mater.* **15**, 601–605 (2016).
49. Schönfeld, C. et al. Dynamical renormalization of the magnetic excitation spectrum via high-momentum nonlinear magnonics. *Sci. Adv.* **11**, eadv4207 (2025).
50. Imada, M., Fujimori, A. & Tokura, Y. Metal-insulator transitions. *Rev. Mod. Phys.* **70**, 1039–1263 (1998).
51. Träger, N. et al. Real-space observation of magnon interaction with driven space-time crystals. *Phys. Rev. Lett.* **126**, 057201 (2021).
52. Troncoso, R. E., Ulloa, C., Pesce, F. & Nunez, A. S. Antiferromagnetic magnonic crystals. *Phys. Rev. B* **92**, 224424 (2015).
53. Streib, S., Vidal-Silva, N., Shen, K. & Bauer, G. E. W. Magnon–phonon interactions in magnetic insulators. *Phys. Rev. B* **99**, 184442 (2019).

Publisher's note Springer Nature remains neutral with regard to jurisdictional claims in published maps and institutional affiliations.

Springer Nature or its licensor (e.g. a society or other partner) holds exclusive rights to this article under a publishing agreement with the author(s) or other rightsholder(s); author self-archiving of the accepted manuscript version of this article is solely governed by the terms of such publishing agreement and applicable law.

© The Author(s), under exclusive licence to Springer Nature Limited 2026

Methods

Sample and experimental set-up

We studied a monocrystalline, 60-µm-thick $DyFeO_3$ sample grown by floating-zone melting. The sample was cut perpendicularly to the z crystallographic axis in the form of a thin slab. The sample was kept in a closed-cycle He cryostat (Montana Instruments), which allowed it to cool down to 10 K and vary the temperature with high stability in a wide temperature range (10–250 K). An amplified 1-kHz Ti:Sapphire laser system (SpitfirePro, Spectra Physics; central wavelength, 800 nm; pulse energy, 4 mJ; pulse duration, 50 fs) forms the basis of the experimental set-up. A large fraction of this output is used to pump an optical parametric amplifier (TOPAS TWINS, LIGHT CONVERSION) and thus to produce pulses at variable photon energy. A small portion of the pulses was sent through a mechanical delay line and used as a probe of the spin dynamics in the reflection and transmission geometries. Pump and probe pulses were focused onto the $DyFeO_3$ sample (pump spot diameter 300 µm; typical fluence 1 mJ cm^{-2}; typical heating by above-bandgap pulse less than 50 K; probe spot diameter 80 µm). The pump-induced changes in the polarization $\theta_{K,F}$ of the reflected or transmitted probe pulse were measured using an optical polarization bridge (Wollaston prism) and a pair of balanced Si photodetectors.

Numerical modelling

The system of coupled evolution equations (for the derivation, see Supplementary Note 2.2) was numerically solved for every site in a system of size $N = 5{,}000$ unit cells (corresponding to 3.8 µm), using the Euler cluster of ETH Zürich. The initial conditions for the equations were taken to be those of the equilibrium canted phase. At the sample edge facing the pump, boundary conditions (one fewer neighbour for each surface site, compared with the bulk) introduce small variations in the equilibrium canting angle, manifesting as a domain wall approximately five unit cells in size. We determine this configuration numerically, by minimizing the energy in Dirac's Lagrangian method, before applying the parameter quench and starting the real-time evolution.

Because the experimental sample is 60 µm thick and the focus of this work is on near-surface effects arising from strong absorption of the pump radiation, we can effectively treat the material as semi-infinite in the $\hat{z}$ direction. At the far edge of the simulated system, we therefore use an absorbing boundary condition, to avoid any unphysical reflection of the propagating wavepackets. This is implemented by adding $N_{\mathrm{boundary}} = 250$ extra sites with progressively higher values of the local damping λ. Afterwards, these sites are not taken into account when recovering the non-equilibrium response of the system.

Data availability

Source data for figures are publicly available via Zenodo at https://doi.org/10.5281/zenodo.18430301 (ref. 54). All other data that support the findings of this Article are available from the corresponding authors upon request. Source data are provided with this paper.

Code availability

The code used to simulate the magnetic dynamics is available from the corresponding authors upon reasonable request.

References

54. Radovskaia, V. et al. Figure source data for 'Photoengineering the magnon spectrum in insulating antiferromagnet'. *Zenodo* https://doi.org/10.5281/zenodo.18430301 (2026).

Acknowledgements

We thank K. Saeedi Ilkhchy and C. Berkhout for their technical support, as well as J. Mentink for fruitful discussions. This work is supported by ERC grant 852050 MAGSHAKE (to R.V.M.); ERC grant 101078206 ASTRAL (to D.A.); programme 'Materials for the Quantum Age' (QuMat, registration number 024.005.006 to A.V.K. and D.A.), which is part of the Gravitation programme financed by the Dutch Ministry of Education, Culture and Science (OCW); and the European Research Council ERC grant agreement no. 101054664 273 (SPARTACUS to A.V.K.). R.C. received support by Horizon Europe EIC Pathfinder under the grant IQARO number 101115190 and from the Italian PNRR MUR project PE0000023-NQSTI. R.A. and E.D. acknowledge the SNSF project 200021_212899, NCCR SPIN, a National Centre of Competence in Research, funded by the Swiss National Science Foundation (grant no. 225153), and the Swiss State Secretariat for Education, Research and Innovation contract no. UeM019-1). The work was partly was supported by the Swiss State Secretariat for Education, Research and Innovation (SERI) under contract no. MB22.00071 (to A.D.C.), the Gordon and Betty Moore Foundation (grant no. 332 GBMF10451 to A.D.C.), the European Research Council (ERC) (grant no. 677458), by the project Quantox of QuantERA ERA-NET Cofund in Quantum Technologies, and by the Netherlands Organisation for Scientific Research (NWO/OCW) as part of the VIDI (project 016.Vidi.189.061 to A.D.C.), the ENW-GROOT (project TOPCORE) programme (to A.D.C.)

Author contributions

D.A. and A.D.C. conceived the project. D.A., A.V.K. and A.D.C. supervised the study. V.R., J.R.H., M.X.N. and D.A. performed the experiments. R.A. and E.D. provided the theoretical model. B.A.I., R.V.M., S.C. and R.C. contributed to the theoretical treatment of the experimental results. D.A., V.R. and R.A. wrote the original draft with feedback from all the co-authors.

Competing interests

The authors declare no competing interests.

Additional information

Extended data is available for this paper at https://doi.org/10.1038/s41567-026-03230-6.

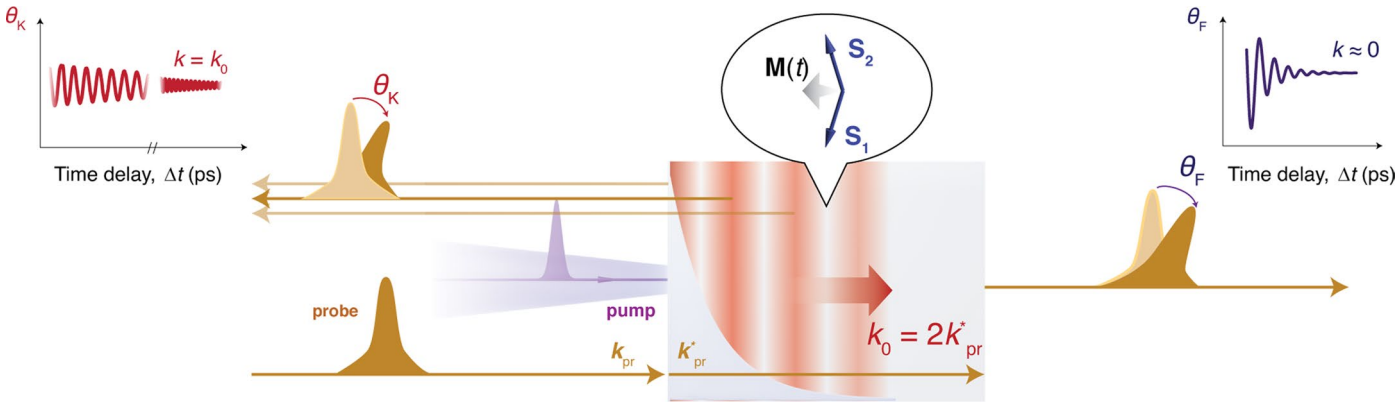
Supplementary information The online version contains supplementary material available at https://doi.org/10.1038/s41567-026-03230-6.

Correspondence and requests for materials should be addressed to V. Radovskaia or D. Afanasiev.

Peer review information *Nature Physics* thanks Romain Lebrun, Alexej Pashkin and the other, anonymous, reviewer(s) for their contribution to the peer review of this work.

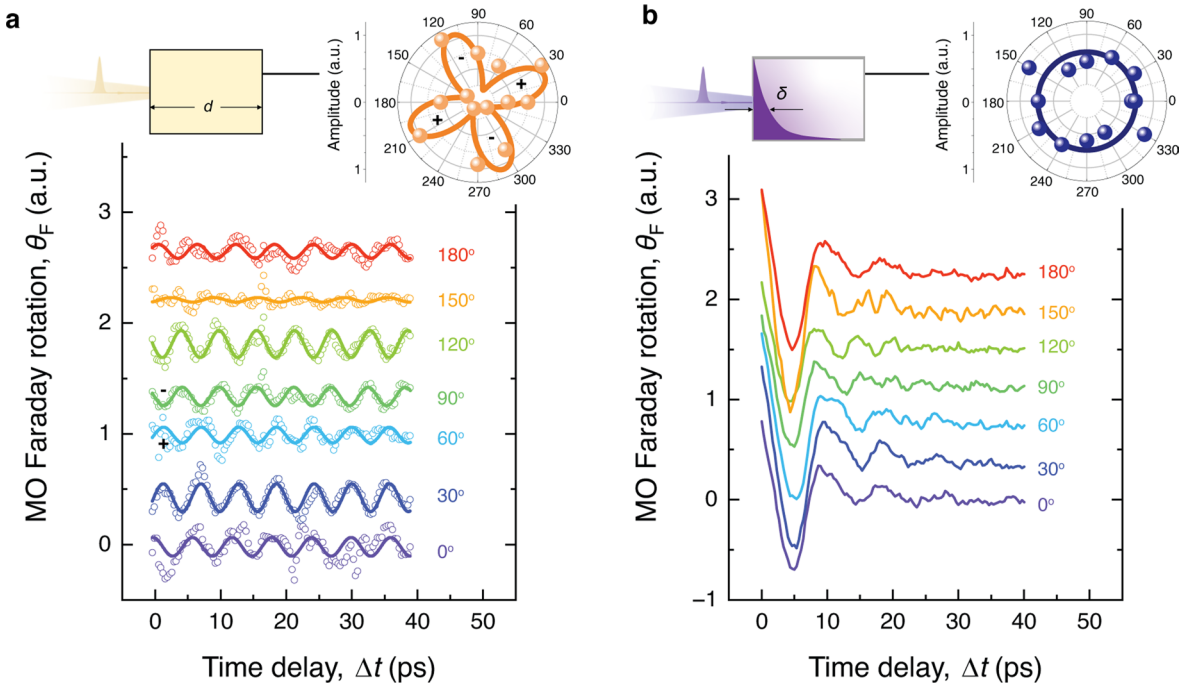
Reprints and permissions information is available at www.nature.com/reprints.

https://doi.org/10.1038/s41567-026-03230-6



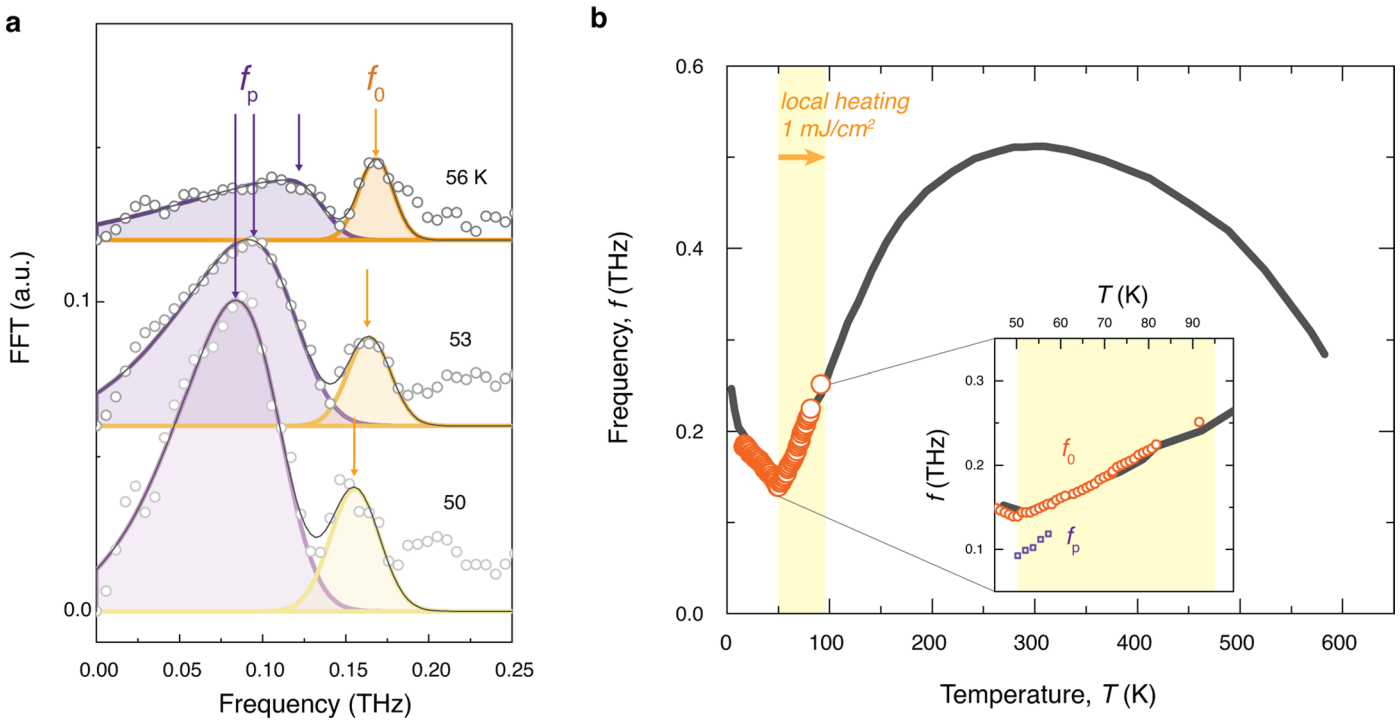
Extended Data Fig. 1 | Schematics of the experiment. The time-resolved signals (illustrated schematically at the top-left and top-right) were obtained using a pump-probe technique. The first, pump pulse (purple) excites the near-surface region (depicted as the blue area with exponential profile), and the second, probe pulse with wavevector $\boldsymbol{k}_{pr}$ (orange, bottom-left) measures the magnetic response. When transmitted through the medium, the probe pulse experiences a magneto-optical Faraday rotation θ_F of its polarization due to the net magnetization $\mathbf{M}(t)$ (shown enlarged in the inset), thus providing information about localized magnon dynamics with $k \approx 0$ (middle-right; purple colour). The refracted portion of the probe pulse acquires a new wavevector $\boldsymbol{k}^*_{pr}$ within the sample, and is subsequently reflected by inhomogeneities possessing a spatial periodicity matching – specifically, magnons with the wavevector $\boldsymbol{k}_0 = 2\boldsymbol{k}^*_{pr}$ (schematically shown as red 'waves'). The polarization rotation of this reflected portion is the magneto-optical Kerr rotation θ_K, which provides insights into propagating magnons with wavevector $\boldsymbol{k}_0$ (top-left; red color).

https://doi.org/10.1038/s41567-026-03230-6



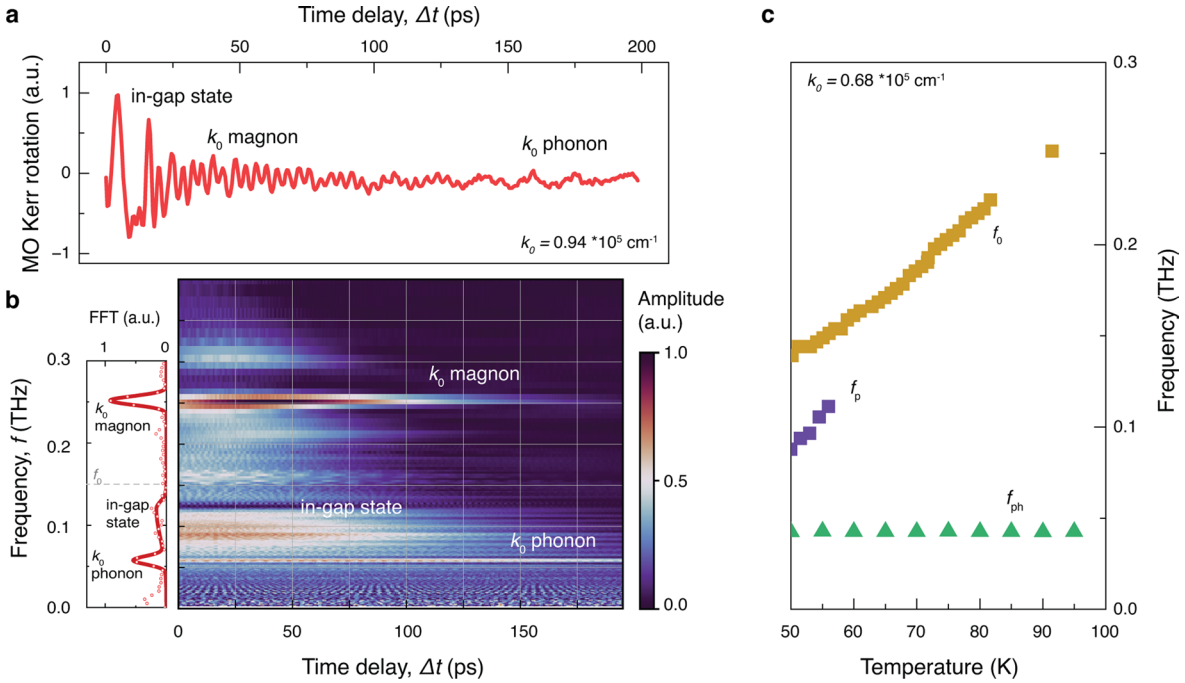
Extended Data Fig. 2 | Pump-polarization dependence. Time-traces for the $k \approx 0$ dynamics excited by linearly-polarized pump with different orientation of polarization when pumping **(a)** not in *CT*-regime and **(b)** in *CT*-regime. On the panel (a) the scatters are experimental data points and solid lines are sinusoidal fits. On panel (b) solid lines are the experimental time-traces. Labels from 0^0 to 180^0 denote the orientation of the pump polarization for every particular curve. Top-left insets on both graphs show the spatial distribution of the excitation. Top-right insets are the dependences of the amplitude from the angle of the pump polarization. While in *CT*-regime (b) the magnetic dynamics is isotropic, in off-resonant regime (a) the orientation of pump polarization allows to control not only the amplitude of the dynamics, but also the phase (compare '+' light-blue and '-' dark-green curves).

https://doi.org/10.1038/s41567-026-03230-6



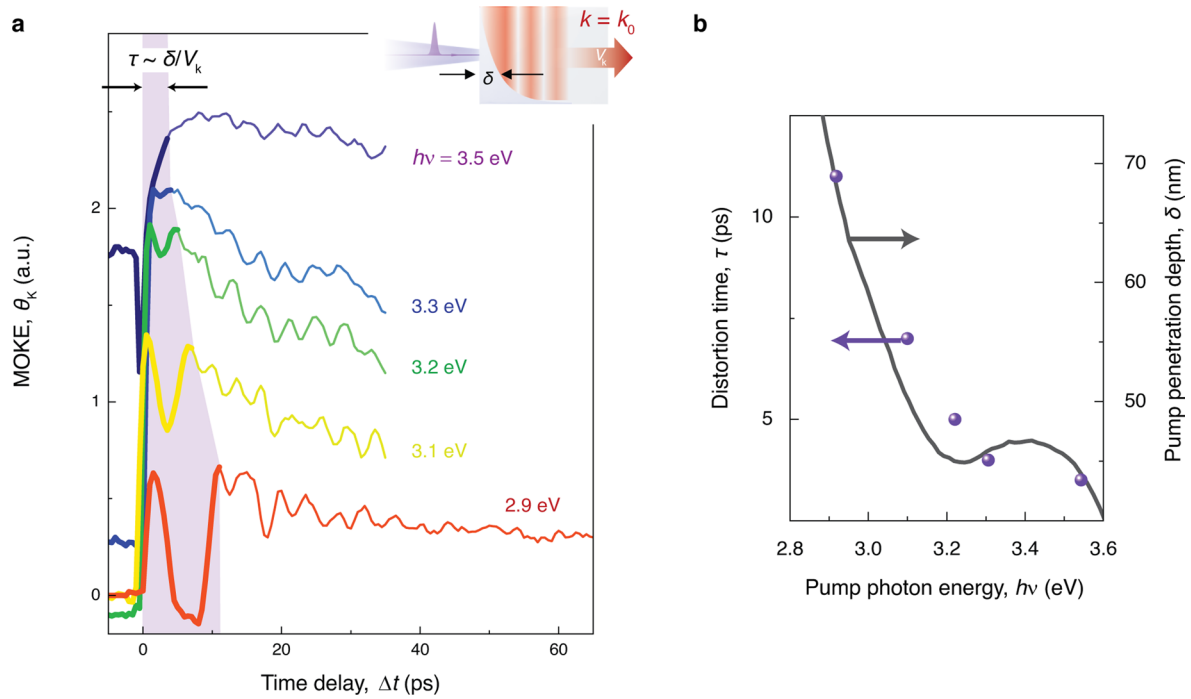
Extended Data Fig. 3 | Temperature-evolution of the localized k ≈ 0 magnon state. (a) Fourier spectra of the unperturbed equilibrium (orange color) and *CT*-excitation-modulated part (purple) part of the localized $k \approx 0$ magnon mode for different temperatures ($T = 50, 53, 56$ K). Black solid lines are the fits taken as a sum of asymmetrical gaussian (purple filled peaks) and symmetrical gaussian (orange filled peaks) at frequencies f_p and f_0, respectively. **(b)** The frequencies f_0 and f_p plotted as a function of temperature. Inset is a zoom-in of range from 45 K to 100 K. Orange-edge circles and purple-edge squares are experimental data points for $h\nu < E_{CT}$ and $h\nu < E_{CT}$, respectively. Black solid line is the adaptation from[39]. Yellow shadow area with orange arrow represents the heating in the local excited area by above *CT*-bandgap laser pulse with pump fluence 1 mJ/cm^2.

https://doi.org/10.1038/s41567-026-03230-6



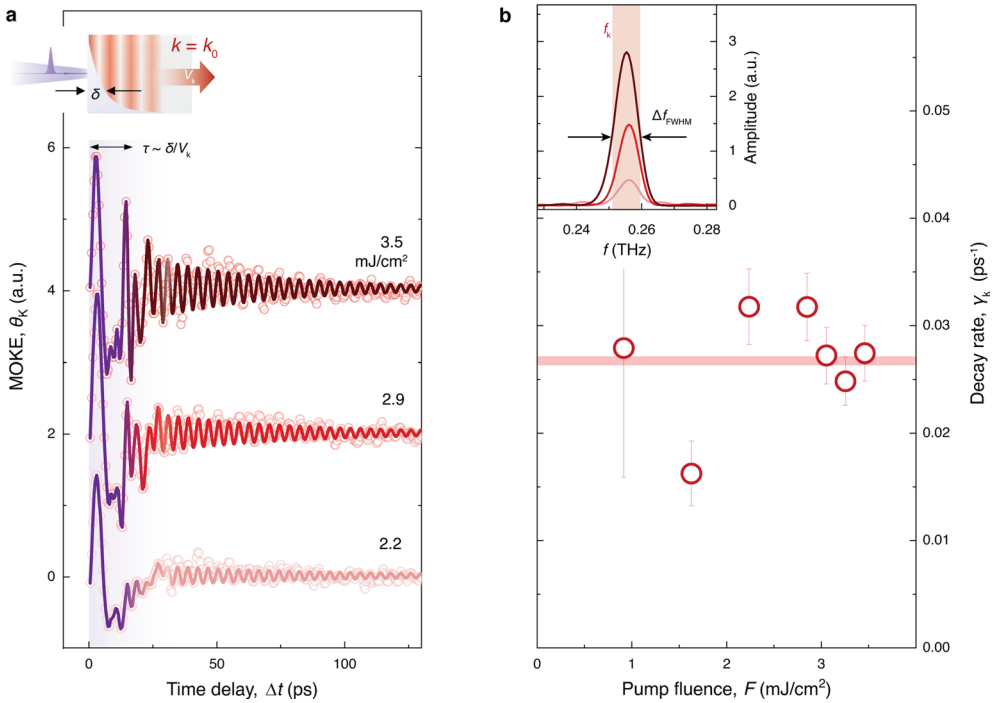
Extended Data Fig. 4 | Simultaneous detection of magnon and phonon. **(a)** Time-resolved trace of the MO Kerr rotation θ_K probing the coherent dynamics excited by the above-bandgap pump excitation ($h\nu = 3.1$ eV). The parameters were set to: $\lambda_{pr} = 515$ nm ($k_0 = 0.94{*}10^5\,cm^{-1}$) $T \approx 60$ K. **(b)** (left panel) Fourier spectrum and (right panel) the wavelet analysis of the signal from (a). Three main states can be distinguished: k_0 phonon peak (≈ 0.06 THz), k_0 magnon peak (≈ 0.25 THz) and the in-gap state originating from the early-time distortion (≈ 0.1 THz). **(c)** Temperature-dependence for the frequency of the equilibrium $k \approx 0$ magnons f_0, in-gap state f_p and acoustic phonon at $k_0 = 0.68{*}10^5\,cm^{-1}$ ($\lambda_{pr} = 670$ nm).

https://doi.org/10.1038/s41567-026-03230-6



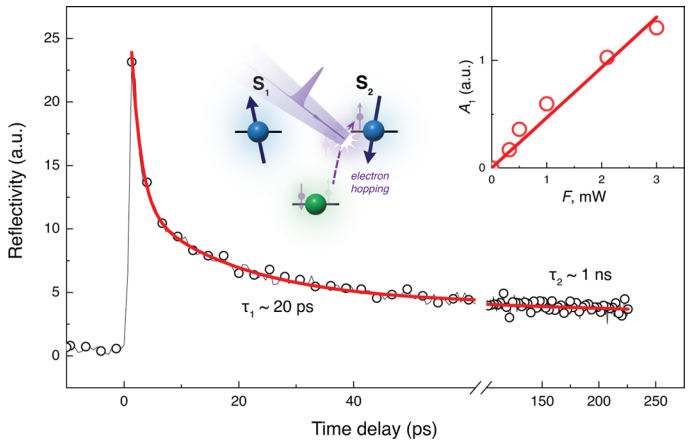
Extended Data Fig. 5 | The effect of pump photon energy on the duration of early-time distortion in the dynamics of propagating finite-k components. **(a)** Time-resolved traces of the magneto-optical Kerr rotation (MOKE) θ_k excited by pumping with different pump photon energies $h\nu$ from 2.9 eV up to 3.5 eV. The bold part of the curves, as well as purple shaded area, highlights the distorted early-time magnon dynamics with a duration of τ. Top right inset shows a spatial distribution of the probed magnon dynamics; δ is a pump penetration depth. **(b)** τ (left axis, circles) and δ (right axis, solid line) as a function of pump photon energy $h\nu$. Here τ was determined by visual inspection of the start-time of coherent oscillations from (a).

https://doi.org/10.1038/s41567-026-03230-6



Extended Data Fig. 6 | Pump fluence-independent decay rate of propagating finite-k magnons. (a) Time-traces of $k = k_0$ magnon mode for different fluences of the above-bandgap pump excitation ($h\nu = 3.1$ eV). The inset schematically shows spatial localization of the measured dynamics; δ is the pump penetration depth; V_k is the group velocity of the propagating magnon. Purple shady area, as well as purple color of curves, highlights early-time τ distorted dynamics. **(b)** (circles) Experimental values of the decay rate of *CT*-driven $k = k_0$ magnon mode, γ_k, as a function of pump fluence. Red solid line is guide-to-eye. Error bars indicate 1σ uncertainties from nonlinear least-squares fitting. (inset) Fourier peak of late-time coherent part of $k = k_0$ mode for different pump fluences. Neither the central frequency of the peak $f_k \approx 0.25$ THz (highlighted by shady red stripe), nor the FWHM bandwidth $\Delta f_{FWHM} \approx 0.01$ THz are affected by the pump-fluence.

https://doi.org/10.1038/s41567-026-03230-6



Extended Data Fig. 7 | Lifetime of CT electronic excitation induced by light. Time-resolved dynamics of the transient reflectivity following the ultrafast *CT* excitation. Circles represent experimental data points, and the red line shows a three-exponential fit with relaxation times: $\tau_0 \approx 1$ ps, $\tau_1 \approx 20$ ps and $\tau_2 \approx 1$ ns. The last two time constants suggest that the non-equilibrium behavior of the photoexcited carriers extends far beyond the ≈7 ps lifetime of the spin precession. The central inset is a schematic representation of the *CT* electronic excitation. The top-right inset is the fluence-dependence of the amplitude A_1 of the τ_1 exponent. Open circles are the experimental values, and the straight solid line is a linear fit.